agronomy

MDPI

Article

Predicting Soil Temperature and Quantifying Thermal Effects of Straw Mulching via a Data-Physics Dual-Driven Neural Network (Hy-PINN)

Fangyuan Zhang, Dinghai Xia, Bo Chen, Junjie Xia and Ren Zhang *

College of Engineering, Shenyang Agricultural University, Shenyang 110866, China
* Correspondence: zr001@syau.edu.cn; Tel.: +86-18624404110

Abstract

Soil temperature is a critical meteorological factor influencing crop growth. Given that the dynamics of soil temperature under various straw mulching practices remain unclear, a two-year field experiment (2024–2025) was conducted. Four treatments were established—no mulching (CK), chopped straw mulching (CS), strip tillage (SS), and whole straw mulching (WS). Results indicated that straw mulching significantly altered the soil thermal environment; the cooling intensity followed the order of WS > SS > CS (averaging 0.58–1.72 °C) and was primarily concentrated during the seedling stage (1.09–2.82 °C). While full-scale mulching may induce early cold stress, SS mitigated this effect, providing a more balanced thermal environment. To address the reliance of traditional physical models on soil boundary conditions and parameters, we proposed a data-physics dual-driven hybrid physics-informed neural network (Hy-PINN). This model simultaneously predicts soil temperatures at 0 cm and 10 cm depths and dynamically inverts the apparent thermal diffusivity (κ). Through strict cross-year evaluation (training on 2024, independent testing on 2025), the Hy-PINN achieved high-precision predictions across all scenarios ($R^2 \geq 0.89$; RMSE ≤ 0.95 °C at 0 cm and $\leq$1.10 °C at 10 cm). The Hy-PINN model serves as a robust complementary tool to field monitoring, providing a scientific basis for assessing the thermal suitability of conservation tillage patterns.

Keywords: deep learning; physics-informed neural network (PINN); heat conduction equation; thermal diffusivity; straw mulching

1. Introduction

Soil temperature is a critical environmental factor in conservation tillage systems, directly affecting crop phenology [1], canopy development, and yield formation [2]. Conservation tillage has been widely adopted in semi-arid black soil regions, playing a vital role in promoting ecological restoration, enhancing cultivated land quality, and ensuring agricultural sustainability. As the core technology of conservation tillage, straw mulching regulates energy and water exchange within the soil-crop system, thereby improving the thermal environment [3,4] and hydrological conditions in the root zone, which ultimately promotes crop growth and increases yield [5]. However, the regulatory effects of straw mulching patterns with varying morphological and spatial distributions—such as whole straw mulching (WS), chopped straw mulching (CS), and strip tillage (SS)—on the soil thermal environment exhibit significant spatiotemporal heterogeneity [6]. For instance, full-scale straw mulching during the spring sowing period often exerts a pronounced cooling effect that delays soil warming, potentially inducing chilling injury and postponing

Check for updates

Academic Editor: Dimitrios D. Alexakis

Received: 2 September 2026
Revised: 18 October 2026
Accepted: 26 October 2026
Published: 8 November 2026

Copyright: © 2026 by the authors. Licensee MDPI, Basel, Switzerland. This article is an open access article distributed under the terms and conditions of the Creative Commons Attribution (CC BY) license.

crop emergence. In contrast, strip tillage attempts to strike an optimal balance between soil moisture conservation and spring warming. Therefore, accurately quantifying soil temperature dynamics across key crop growth stages under various mulching patterns, along with obtaining continuous, high-resolution deep soil temperature data, is a fundamental prerequisite for optimizing sowing windows and tillage decisions [7,8].

Current soil temperature simulation methods are primarily categorized into two approaches: physics-based process models and purely data-driven machine learning models. Traditional physical models—such as HYDRUS-1D [9], SHAW [10], and the force-restore method [11]—calculate soil temperature profiles based on the principles of energy conservation and heat conduction equations. However, when applied to conservation tillage scenarios, these models require the precise input of physical parameters for the straw mulching layer (e.g., porosity and thermal conductivity). Since obtaining these parameters at the field scale is highly costly and exhibits strong spatiotemporal variability, their inherent uncertainties frequently lead to a substantial decline in prediction accuracy.

To overcome the dependence of physical models on boundary conditions and soil thermal diffusivity, data-driven models have garnered widespread attention in recent years [12,13]. Early studies employed algorithms such as support vector machines and random forests to establish nonlinear mappings between meteorological factors and soil temperature [14]. Although recent advancements in deep learning have facilitated the construction of interpretable spatiotemporal deep neural networks [15] to quantify the contributions of environmental factors via component decomposition, these explanations remain confined to statistical correlations, failing to embed fundamental physical laws into the model architecture. Consequently, when confronted with sparse data or extreme climate events, purely data-driven models may yield out-of-distribution predictions that violate physical principles [16–18].

By incorporating partial differential equations (PDEs) into the loss function as regularization terms, Physics-Informed Neural Networks (PINNs) compel the model to adhere to physical laws, thereby achieving an optimal balance between physical rigor and data flexibility [19,20]. In soil physics, previous research has demonstrated the potential of PINNs for inverse estimation of porous-media parameters [21]. A separate study applied PINNs to field soil temperature simulation and reported higher predictive accuracy than both purely physics-based models and purely data-driven deep neural networks (DNNs), without requiring prior thermal parameters [22]. However, most existing PINN research focuses primarily on homogeneous soils or simple boundary conditions, and its applicability in complex conservation tillage scenarios—such as straw mulching—has not yet been systematically evaluated. Furthermore, current models lack the capability to simultaneously predict soil temperatures at multiple depths while dynamically inverting time-varying thermal diffusivity.

To address the aforementioned challenges, the specific objectives of this study are to: (1) systematically evaluate the regulatory effects of various straw mulching practices (CS, SS, and WS) on soil temperature during key growth stages of maize, and quantify the stage-specific temperature differences alongside diurnal dynamic characteristics; and (2) develop a hybrid physics-informed neural network (Hy-PINN) that leverages a data-physics dual-driven approach to resolve the issues of ambiguous surface energy boundaries and soil thermal parameter uncertainties under conservation tillage.

Specifically, the Hy-PINN encompasses a residual learning-based Surface-DNN module to reconstruct the surface boundary temperature, alongside a decoupled parameter projection branch for dynamic inversion. Furthermore, the one-dimensional unsteady heat conduction equation is embedded into the loss function as a physical constraint. Instead of relying on measured soil temperatures as boundary conditions, the model requires only routine meteorological data to simultaneously predict soil temperatures at depths of 0 cm

and 10 cm while inverting the relevant parameters. Utilizing two years of observation data from maize fields in Northeast China under four treatments (CK, CS, SS, and WS), the predictive performance of Hy-PINN and the thermal effects of the various mulching patterns it revealed were evaluated through a cross-year approach (training on 2024 data and independently testing on 2025 data). Ultimately, this study not only provides an accurate and cost-effective method for soil temperature prediction but also offers a quantitative scientific basis for optimizing conservation tillage patterns and sowing decisions.

2. Materials and Methods

2.1. Data Sources

The field experiments were conducted during the 2024 and 2025 growing seasons at the Fuxin Agricultural Experiment Station (42°01′ N, 121°40′ E, altitude 219 m) in Liaoning Province, China, as illustrated in Figure 1. This station is located in a typical semi-arid rainfed agricultural region. The soil profile consists of loam in the 0–20 cm layer and silt loam in the 20–100 cm layer. The physicochemical properties of the soil in the experimental area are detailed in Table 1. The tested maize variety was 'Xiyuan 1908'. The crop was planted with a row spacing of 60 cm and a plant spacing of 30 cm, achieving a planting density of approximately 55,500 plants ha^{-1}. The straw application rate was 7500 kg ha^{-1}. Throughout the entire growing season, the crops were rainfed without any supplemental irrigation. All treatments were maintained under no-tillage conditions. Other field management practices were identical across all treatments and followed local standard agronomic protocols.

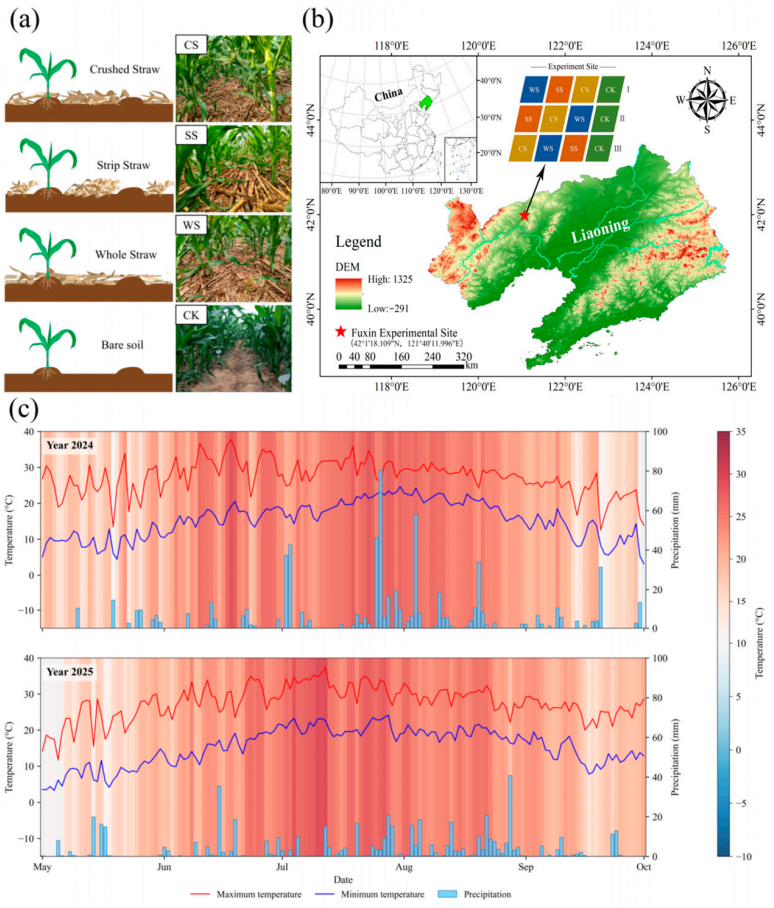


Figure 1. Location of the study area and experimental details: (**a**) schematic diagram of the four straw mulching practices; (**b**) geographical map of the experimental field; (**c**) precipitation distribution in 2024 and 2025.

Table 1. Physicochemical properties of the soil in the study area.

Soil Depth (cm)	Bulk Density ($g \cdot cm^{-3}$)	Organic Matter ($g \cdot kg^{-1}$)	Soil Texture
0–20	1.57	8.74	Loam
20–40	1.45	5.07	Silt loam
40–60	1.42	3.41	Silt loam
60–80	1.43	3.76	Silt loam
80–100	1.47	1.11	Silt loam

During the 2024 maize growing season (April to October), the average temperature was 22.8 °C, and the cumulative precipitation reached 567.8 mm. The precipitation was unevenly distributed; specifically, the cumulative rainfall from July to August amounted to 449.1 mm, accounting for 79.1% of the annual total. The year 2025 was classified as a normal precipitation year with a total rainfall of 530.19 mm, representing a 6.6% decrease compared to 2024. The average temperatures were similar across both years, and extreme high temperatures in both years approached 38 °C, both occurring in mid-July. The dynamic changes in daily maximum temperature, daily minimum temperature, and daily precipitation during the experimental period are illustrated in Figure 1c, which clearly demonstrates the strong interdiurnal meteorological fluctuations and the typical characteristic of concurrent rainfall and heat in the study area.

No-tillage straw mulching is widely adopted as a conservation tillage practice in this region [23,24]. The experiment incorporated the primary local no-tillage mulching methods, establishing four treatments: chopped straw mulching (CS, with straw chopped to lengths of 5–10 cm), strip tillage (SS, featuring alternating straw-mulched and bare soil strips, each approximately 30 cm wide), whole straw mulching (WS, where intact straw was applied), and a no-mulching control (CK) (Figure 1a). A randomized complete block design was employed with three replicates for each treatment, yielding a total of 12 plots. Each plot covered an area of 105 m^2 (7 m × 15 m).

Meteorological data, including air temperature, solar radiation, precipitation, relative humidity, wind speed, evapotranspiration, and atmospheric pressure, were provided by the Fuxin Meteorological Station, located within 500 m of the experimental site, at an hourly recording interval. Soil temperature was continuously monitored using Internet of Things (IoT) temperature and humidity data loggers (GS1-AL4G1RS, Dalian Yundongli Technology Co., Ltd.,Dalian, China). Specifically, UB-STH-N1 sensors based on frequency domain reflectometry (FDR) were installed at depths of 0 cm and 10 cm. These sensors possess an inherent accuracy of ±0.2 °C and were strictly factory-calibrated prior to field installation, ensuring high-fidelity continuous observations. For the mulched treatments, the "0 cm" depth was strictly defined as the interface between the mineral soil surface and the bottom of the straw mulch layer. Soil temperature data were recorded every 20 min via a 4G network (specifically at :00, :20, and :40 of each hour; hence, the minimum resolvable temporal shift for diurnal peak/trough timing is ±20 min, and reported shifts of 20, 40, and 100 min represent discrete multiples of the 20 min sampling resolution). To align with the hourly resolution of the meteorological inputs, the three 20 min soil temperature observations within each hour were first arithmetically averaged at the sensor level, and subsequently averaged across the three replicate plots ($n = 3$) per treatment to generate the representative treatment-level time series. Missing observations or anomalous spikes (<1% of the dataset) were corrected using linear interpolation.

2.2. Components of the Hy-PINN Model

2.2.1. Neural Network Architecture

In this study, a Hy-PINN model was constructed using a fully connected feedforward neural network. The network comprises three hidden layers, each containing 128 neurons, and employs the hyperbolic tangent (tanh) activation function. The input layer receives the normalized values of seven meteorological variables at time step t. The output layer consists of three branches: $\Delta\hat{T}_0(t), \Delta\hat{T}_{10}(t)$ and $z(\kappa(t))$. The network architecture is illustrated in Figure 2.

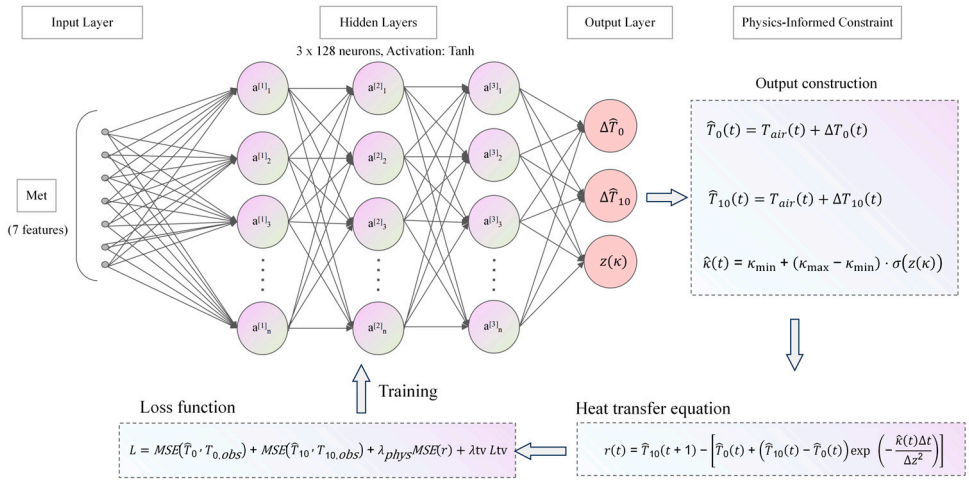


Figure 2. Neural network structure diagram.

Specifically, the data-fitting capability of deep neural networks is leveraged to address complex surface boundary conditions, seamlessly integrating this capability with fundamental physical principles. The input layer of the model receives meteorological data (e.g., air temperature, solar radiation, and precipitation). Subsequently, through multiple fully connected layers, the neurons in each layer extract features and perform nonlinear mappings via weights and activation functions. Ultimately, instead of directly outputting the final soil temperature, the output layer generates a residual term ($\Delta\hat{T}_0$, $\Delta\hat{T}_{10}$) alongside the latent representation of the physical parameters $z(\kappa)$.

$$\Delta\hat{T}_0 = W_{t0}H + b_{t0}$$

$$\Delta\hat{T}_{10} = W_{t10}H + b_{t10}$$

$$z(\kappa) = W_{\kappa}H + b_{\kappa}$$

where $H \in R^{128}$ denotes the shared latent feature vector extracted by the final hidden layer, and W_{t0}, W_{t10}, W_{κ} and b_{t0}, b_{t10}, b_{κ} are the weight matrices and biases of the three decoupled linear output branches, respectively.

Soil temperature deviation: Outputs the temperature deviations at depths of 0 cm and 10 cm relative to the air temperature $\Delta\hat{T}$.

Thermal diffusivity $z(\kappa)$: Outputs the dynamic predictions utilized to construct the thermal diffusivity.

While a unified Hy-PINN architecture was employed across all scenarios, the network weights were trained independently for each of the four treatments (CK, CS, SS, and WS) using their respective datasets. This treatment-specific training approach was necessary to accurately capture the distinct surface boundary conditions and thermal dynamics induced by the specific physical morphologies of the mulches, rather than training a single universal model.

2.2.2. Overview of the Surface-DNN Module

The input layer integrates seven key environmental variables—air temperature, solar radiation, precipitation, relative humidity, wind speed, evapotranspiration, and atmospheric pressure—to comprehensively capture the physical elements governing soil thermal processes.

To enhance prediction stability and ensure the validity of the physical parameters, given the strong autocorrelation between surface temperature and air temperature, directly predicting absolute temperatures often traps the model in local optima and leads to slow convergence.

This study introduces a residual learning strategy: utilizing the air temperature $T_{air}(t)$ as a baseline and superimposing the deviation values predicted by the network, the final temperature predictions are derived as follows:

$$\hat{T}_0(t) = T_{air}(t) + \Delta\hat{T}_0(t)$$

$$\hat{T}_{10}(t) = T_{air}(t) + \Delta\hat{T}_{10}(t)$$

2.2.3. Dynamic Thermal Diffusivity Prediction Module

This module addresses a typical inverse problem: inversely inferring soil thermal properties from the evolution of the temperature field in the absence of measured parameters.

Decoupled parameter projection branch: Constructing a dedicated output projection head ($z(\kappa) = W_\kappa H + b_\kappa$) decoupled from the temperature residual heads (ΔT_0 and ΔT_{10}) avoids direct output-layer gradient interference during multi-task learning, thereby enabling the model to stably extract the evolutionary patterns of soil thermal properties from the shared latent representation.

Physical parameter constraints: To ensure that the inverted apparent thermal diffusivity consistently remains within a reasonable physical range $[\kappa_{\min},\kappa_{\max}]$, a Sigmoid transformation is applied to the variable $z(\kappa)$ as follows:

$$\hat{\kappa}(t) = \kappa_{\min} + (\kappa_{\max} - \kappa_{\min}) \cdot \sigma(z(\kappa))$$

where $\sigma(.)$ is the Sigmoid activation function.

Guided by prior knowledge from classical soil thermophysics (e.g., the thermal diffusivity of typical agricultural soils generally ranges from 0.2×10^{-6} to 2.0×10^{-6} m^2/s), the computational boundaries for thermal diffusivity were established as follows during model construction. Specifically, these boundaries were set to $\kappa_{\min} = 0.2 \times 10^{-6}$ $m^2 \cdot s^{-1}$ and $\kappa_{\max} = 2.0 \times 10^{-6}$ $m^2 \cdot s^{-1}$. Note that in the numerical implementation, an internal scaling factor of 10^3 was applied to normalize gradient magnitudes, which has been rescaled back to standard physical *SI* units ($m^2 \cdot s^{-1}$) in all reported figures. Given the vertical layer spacing of $\Delta z = 0.10$ m, the inverted diffusivity range (1.13×10^{-6} to 1.40×10^{-6} $m^2 \cdot s^{-1}$) corresponds to a characteristic thermal relaxation time ($\tau = \Delta z^2/\kappa$) of 1.98–2.46 h, which physically governs the hourly to diurnal conductive damping and phase lag between the 0 cm and 10 cm soil layers.

2.2.4. Physical Constraint Formulation

Assuming negligible convection and phase transitions, vertical soil heat transfer is described by the one-dimensional unsteady heat conduction equation:

$$\frac{\partial T}{\partial t} = \frac{\partial}{\partial z}\left(\kappa(\theta,t)\frac{\partial T}{\partial z}\right)$$

To ensure the physical interpretability of the model, the dynamic changes in soil temperature along the depth direction must satisfy the one-dimensional vertical heat diffusion process. To derive a tractable physical constraint between the 0 cm and 10 cm layers without requiring deeper soil profile measurements, this study introduces an exponential approximation formulation. Specifically, this derivation is established upon three strict physical assumptions: (1) the apparent thermal diffusivity (κ) is uniformly distributed within the 0–10 cm depth and remains constant during a single time step; (2) the initial temperature profile exhibits an approximately linear distribution; and (3) the upper boundary condition (surface temperature) within this time step is maintained as a constant driver [19].

Applying a finite-volume control-layer approximation over the active topsoil control volume $z \in [z_0, z_1]$ (where $\Delta z = z_1 - z_0 = 0.1$ m), we integrate the one-dimensional unsteady heat conduction equation over this control layer.

$$\int_{z_0}^{z_1} \frac{\partial T}{\partial t} dz = \kappa(t) \frac{\partial T}{\partial z}\bigg|_{z_1} - \kappa(t) \frac{\partial T}{\partial z}\bigg|_{z_0}$$

Applying a lumped-capacitance approximation, the rate of heat storage in the control layer is represented by $\Delta z \frac{dT_{10}(t)}{dt}$ (note that if a linear profile average $\overline{T} = [T_0(t) + T_{10}(t)]/2$ is adopted under slowly varying upper-boundary steps, the constant geometric shape factor of 1/2 is directly absorbed into the effective apparent thermal diffusivity $\kappa(t)$ without altering the relaxation structure). The downward conductive heat flux from the surface (z_0) to the 10 cm layer (z_1) is approximated by a first-order finite difference: $q_{\text{in}} \approx -\kappa(t) \frac{T_{10}(t) - T_0(t)}{\Delta z}$. Because temperature measurements below 10 cm are unavailable in this two-depth configuration, a quasi-adiabatic lower boundary closure is introduced. Specifically, the residual basal heat exchange at z_1 is assumed to be negligible or intrinsically absorbed into the effective relaxation rate of the topsoil layer, meaning the explicit lower boundary flux $q_{\text{out}} \approx 0$. Substituting these approximations into the integrated flux balance and dividing both sides by Δz yields a first-order ordinary differential equation (*ODE*):

$$\frac{dT_{10}(t)}{dt} = -\frac{\kappa(t)}{\Delta z^2}[T_{10}(t) - T_0(t)]$$

Assuming that the apparent thermal diffusivity $\kappa(t)$ and the upper boundary driver $T_0(t)$ remain quasi-constant over a single discrete time step $[t, t + \Delta t]$, separating variables and integrating this *ODE* from t to $t + \Delta t$ gives:

$$\int_{T_{10}(t)}^{T_{10}(t+\Delta t)} \frac{dT_{10}}{T_{10} - T_0(t)} = \int_t^{t+\Delta t} -\frac{\kappa(t)}{\Delta z^2} dt$$

$$\ln\left[\frac{T_{10}(t + \Delta t) - T_0(t)}{T_{10}(t) - T_0(t)}\right] = -\frac{\kappa(t)\Delta t}{\Delta z^2}$$

Taking the exponential of both sides and rearranging yields the exact analytical update over the time step:

$$T_{10}^{\text{phys}}(t + 1) = T_0(t) + [T_{10}(t) - T_0(t)]\exp\left(-\frac{\kappa(t)\Delta t}{\Delta z^2}\right)$$

Here, the discrete time step is set to $\Delta t = 1$ h (3600 s) to match the hourly meteorological forcing resolution, yielding a dimensionless step-to-relaxation ratio of $\Delta t/\tau \approx 0.41$–$0.51$ that ensures well-conditioned exponential decay and satisfies the quasi-constant step boundary assumption. This exponential form serves as a first-order thermal relaxation model derived from the exact analytical solution of the heat conduction equation under constant boundary conditions [25]. It is important to note that this formulation relies on several simplifying assumptions, including uniform thermal properties within the step and a neglect of explicit upward heat fluxes from soil layers below 10 cm. Therefore, the inverted parameter κ in this

study should be strictly interpreted as an "effective or apparent thermal diffusivity," which intrinsically compensates for unmodeled lower-boundary heat exchanges and moisture-induced variations under field conditions. Based on this, the formulation is incorporated as a physical constraint, defining the residual as follows:

$$r(t+1) = T_{10}(t+1) - T_{10}^{\text{phys}}(t+1)$$

2.2.5. Loss Function

To drive the network to simultaneously learn data features and physical laws, a total loss function incorporating multiple constraints was formulated. The total loss function consists of the following components:

Surface temperature fitting loss:

$$\mathcal{L}_0 = MSE\left(\hat{T}_0, T_{0,obs}\right)$$

10 cm temperature fitting loss:

$$\mathcal{L}_{10} = MSE\left(\hat{T}_{10}, T_{10,obs}\right)$$

Physical consistency constraint loss:

$$\mathcal{L}_{phys} = MSE(r)$$

To suppress unreasonable oscillations, a total variation regularization term is introduced for the temporal variations of κ:

$$\mathcal{L}_{tv} = \sum_t |\hat{\kappa}(t+1) - \hat{\kappa}(t)\,|$$

The final loss is defined as follows:

$$\mathcal{L} = \mathcal{L}_0 + \mathcal{L}_{10} + \lambda_{\text{phys}}\mathcal{L}_{\text{phys}} + \lambda_{\text{tv}}\mathcal{L}_{\text{tv}}$$

where λ_{phys} and λ_{tv} are the weighting coefficients. To balance the gradient magnitudes among the various loss terms, hyperparameter grid search and trial-and-error tuning were employed, ultimately setting the weight values to $\lambda_{phys} = 1.0$ and $\lambda_{\text{tv}} = 1000$ (evaluated on the internally 10^3-scaled diffusivity so that the regularization term is balanced to the same order of magnitude as the temperature MSE losses). T_{obs} denotes the field-measured soil temperature, and MSE represents the mean squared error (MSE) function, which is standardly defined as follows:

$$MSE = \frac{1}{N}\sum_{i=1}^{N}\left(T_{obs,i} - \hat{T}_i\right)^2$$

where N is the total number of samples in the time series, $T_{obs,i}$ is the field-measured soil temperature at the i-th time step, and $\hat{T}_i$ is the corresponding temperature predicted by the network.

2.3. Model Training Strategy

The model was implemented using the PyTorch 2.0 framework and optimized with the Adam optimizer. The initial learning rate was set to 0.002, and a step decay strategy (StepLR) was adopted, which reduced the learning rate by a factor of 0.5 every 1000 epochs. To ensure the full reproducibility of the modeling workflow, the random seed was fixed at 42 across all computational experiments.

To ensure a rigorous evaluation and prevent data leakage, the 2024 dataset was partitioned into a training set (80%) and a validation set (20%), while the entire 2025 dataset

was strictly held out as an unseen independent test set. Specifically, after quality control and meteorological alignment across the maize growing season, the 2024 dataset comprised 4032 continuous hourly records ($N = 168$ days) per treatment, and the 2025 independent test set comprised 3792 continuous hourly records ($N_{\text{test}} = 158$ days) per treatment.

To strictly preserve the 1 h temporal adjacency ($t \rightarrow t + \Delta t$, where $\Delta t = 3600$ s) required for evaluating the physical relaxation residual ($\mathcal{L}_{\text{phys}}$) and total variation regularization ($\mathcal{L}_{\text{tv}}$), a full-batch chronological forward-propagation strategy was employed. During each training epoch, the complete chronological hourly sequence of 2024 (4032 steps) was fed into the network simultaneously so that finite-difference temporal transitions remained unbroken. Supervised data-fitting losses ($\mathcal{L}_0$ and $\mathcal{L}_{10}$) were then evaluated via a daily block boolean mask: $N_{\text{train}} = 134$ days (3216 hourly records, 80%) were used for gradient backpropagation, and $N_{\text{val}} = 34$ days (816 hourly records, 20%) were used exclusively for hyperparameter tuning and early stopping (triggered if the validation RMSE failed to decrease for 200 consecutive epochs). Through grid search ($\lambda_{\text{phys}} \in \{0.1,1,10\}$ and $\lambda_{\text{tv}} \in \{10,100,1000\}$), the optimal weights were established as $\lambda_{\text{phys}} = 1.0$ and $\lambda_{\text{tv}} = 1000$. For seasonal scatter regressions and cross-year summary metrics, hourly predictions and observations were aggregated into matched daily means ($N = 168$ in 2024; $N_{\text{test}} = 158$ in 2025) to evaluate synoptic-scale generalization, whereas unaggregated hourly validation windows were extracted to examine diurnal amplitude attenuation and phase lag fidelity. Because the one-dimensional sequence matrix is compact, full-batch training required approximately 2 min for 3000 epochs on a single NVIDIA RTX 3090 GPU, with single-step inference taking ~1 ms.

2.3.1. Data Preprocessing and Normalization

To eliminate the impact of varying physical dimensions (e.g., solar radiation in W m^{-2} and relative humidity in %) on gradient descent, the Z-Score standardization method was employed to preprocess all input features. The formulation is expressed as follows:

$$x' = \frac{x - \mu}{\sigma}$$

where μ and σ denote the mean and standard deviation of the training set features, respectively. Specifically, it should be noted that during preprocessing, the validation and test sets (2025 data) were standardized strictly utilizing the means (μ) and standard deviations (σ) derived from the training set (2024 data). This rigorous data isolation strategy ensured that the statistical distribution information of the test samples remained completely invisible to the model during the training phase, thereby guaranteeing the objectivity and reliability of the cross-year generalization evaluation.

2.3.2. Statistical Analysis

To quantitatively evaluate the accuracy and reliability of the soil temperature predictions generated by the Hy-PINN model under various mulching scenarios, the coefficient of determination (R2), the root mean square error (RMSE), and the mean absolute error (MAE) were selected as the core statistical evaluation metrics. The specific calculation formulas are expressed as follows:

$$R^2 = 1 - \frac{\sum_{i=1}^{N}(y_i - \hat{y}_i)^2}{\sum_{i=1}^{N}(y_i - \overline{y})^2}$$

$$RMSE = \sqrt{\frac{1}{N}\sum_{i=1}^{N}(y_i - \hat{y}_i)^2}$$

$$MAE = \frac{1}{N}\sum_{i=1}^{N}|y_i - \hat{y}_i|$$

To avoid pseudoreplication, statistical analyses comparing the thermal effects of different treatments (e.g., ANOVA and Tukey's test) were performed using the SciPy library in Python 3.11, with a significance threshold of $p < 0.05$, using daily or growth-stage aggregated mean temperatures at the plot level (n = 3 biological replicates), rather than treating high-frequency observations as independent samples.

3. Results

3.1. Effects of Different Mulching Treatments on the Spatiotemporal Dynamics of Soil Temperature

3.1.1. Seasonal Variation Characteristics of Soil Temperature

Surface mulching significantly altered the soil thermal dynamics, generally manifesting as a cooling effect during the spring warming phase and a heat preservation effect during the autumn cooling phase, with the cooling effect being more pronounced than the heat preservation effect (Figure 3). During the 2024 growing season (April to October), the average soil temperature at the 0 cm depth under the CK treatment was 21.35 ± 4.42 °C (SD). Compared to the CK, the CS, SS, and WS treatments significantly decreased the average soil temperature by 0.58 °C, 0.70 °C, and 1.01 °C, respectively ($p < 0.05$, Tukey's test), among which the WS treatment exhibited the strongest cooling effect. In 2025, the average temperature for the CK treatment was 22.10 ± 3.63 °C, while the average temperatures for the mulching treatments ranged from 20.38 to 21.28 °C. The magnitude of cooling further increased compared to that in 2024, with the WS treatment lowering the temperature by 1.72 °C compared to the CK ($p < 0.01$).

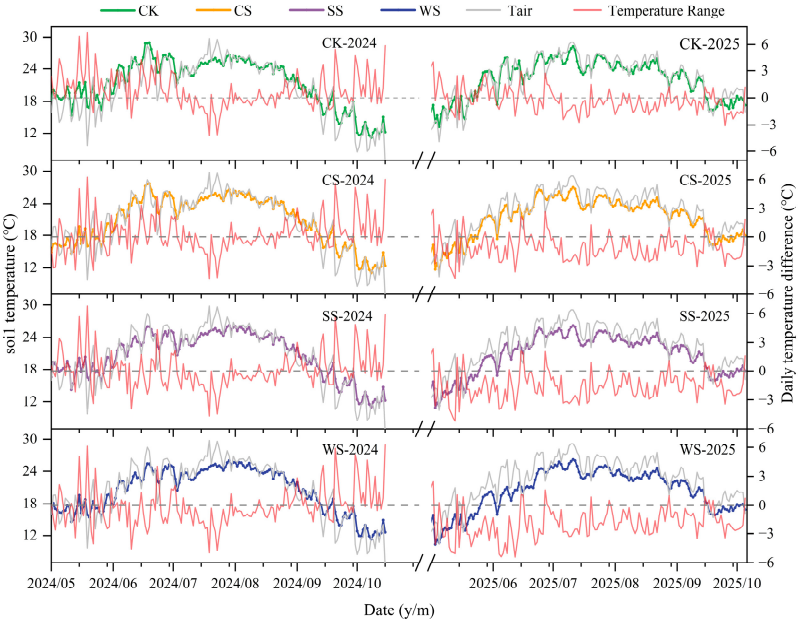


Figure 3. Seasonal dynamics of soil temperature at the 0 cm depth under different mulching treatments from 2024 to 2025.

The temperature difference between the soil and the air under the mulching treatments exhibited dynamic variations as the growth period progressed [26,27]. During the early growth stage (late April to May), the soil temperature under the CK treatment was generally higher than the air temperature because the bare soil surface directly received solar radiation. In contrast, the mulching treatments suppressed soil warming through physical shading, resulting in soil temperatures that were generally lower than the air temperatures, with the WS treatment exhibiting the maximum temperature difference. Entering the middle growth stage (June to July), which was characterized by canopy closure, the soil temperatures in

both the CK and mulching treatments were lower than the air temperature due to canopy shading; however, the mulching treatments continued to exert a superimposed cooling effect. During the late growth stage (September to October), as the canopy senesced, the difference between the soil and air temperatures gradually narrowed and tended to converge [28,29]. These dynamic characteristics demonstrate that the regulation of soil temperature by mulching treatments is distinctly phase-dependent, thereby providing crucial constraints for subsequent model construction.

3.1.2. Variations in Soil Temperature Across Different Growth Stages

To elucidate the impact of different straw mulching practices on maize growth stages, the maize growth period was divided into four key stages: sowing to emergence (SD–VE), emergence to the sixth-leaf stage (VE–V6), sixth-leaf to tasseling stage (V6–VT), and tasseling to physiological maturity (VT–R6). The dynamic characteristics of the surface soil temperature at the 0 cm depth for each treatment across the different growth stages are illustrated in Figure 4. The SD–VE stage is the period when seedlings are most sensitive to soil temperature, with 18–20 °C being the optimal range for seedling growth. This stage represented the lowest temperature interval of the entire growth period. In 2024, the mulching treatments resulted in an average temperature reduction ranging from 1.09 to 2.76 °C, with the average temperature falling between 16.14 and 18.90 °C. In 2025, the magnitude of temperature reduction slightly increased to 1.54–2.82 °C (lowering the temperature by 1.54 °C, 2.32 °C, and 2.82 °C under CS, SS, and WS, respectively), with the treatment mean temperatures ranging from 13.52 to 16.34 °C. Across both years, the differences between the mulching treatments and the CK group were highly significant ($p < 0.001$). Notably, the average temperature of the WS treatment during the SD–VE stage in 2025 was only 13.52 °C (compared to 14.02 °C under SS and 14.80 °C under CS), which closely approached the minimum critical temperature for maize emergence (12 °C). Such a low-temperature environment may lead to delayed emergence and uneven seedling vigor. During the VE–V6 stage, as the air temperature increased, the temperature difference fluctuated the most across the entire growth period. Although the cooling effect weakened, the cooling pattern observed during the seedling stage persisted, with the temperature reduction ranging from 1.16 to 2.54 °C. During this stage, the temperature difference between the CS and SS treatments did not reach a significant level in either year ($p > 0.05$). The V6–VT stage recorded the highest temperatures of the entire growth period, accompanied by reduced fluctuations in temperature differences. The average soil temperature across the different treatments ranged from 23.77 to 25.46 °C. Influenced by canopy shading, the inter-group differences were further minimized, and the direct limiting effect of soil temperature variations on maize vegetative growth gradually diminished. During the VT–R6 stage, there were generally no significant differences among the groups over the two years ($p > 0.05$). By this point, the maximum canopy coverage had been reached, and the crop had entered the reproductive growth stage, resulting in a relatively lower sensitivity to temperature stress. However, it is noteworthy that the WS treatment still maintained a significant difference compared to the CK in 2025 ($p < 0.05$).

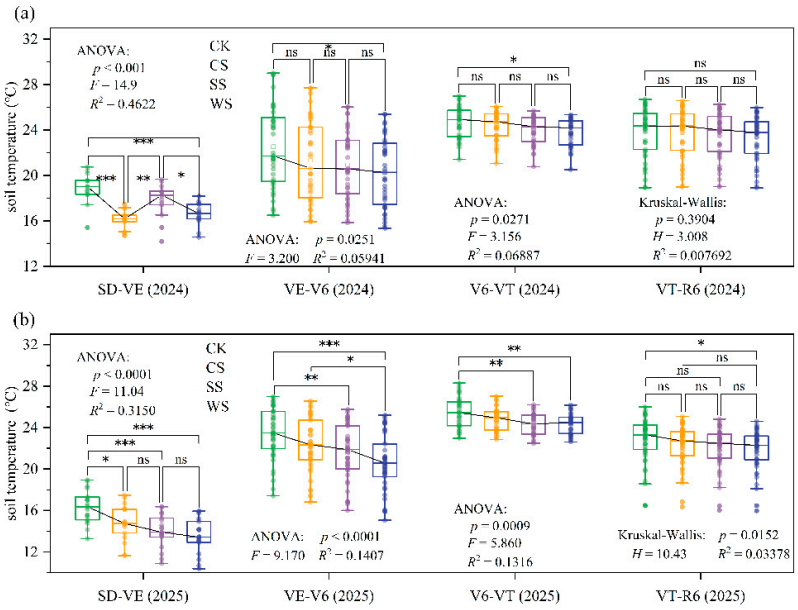


Figure 4. Distribution characteristics of soil temperature at a depth of 0 cm across different maize growth stages under various straw mulching practices in (**a**) 2024 and (**b**) 2025. The symbols *, **, and *** indicate statistically significant differences at $p < 0.05$, $p < 0.01$, and $p < 0.001$, respectively, whereas ns indicates no statistically significant difference ($p \geq 0.05$).

3.1.3. Diurnal Dynamics of Surface Soil Temperature

The diurnal warming and cooling processes of soil temperature serve as the most direct manifestations of the surface energy budget, hydrothermal transfer, and the crop root zone environment. Relying solely on static indicators, such as daily mean and extreme temperatures, makes it difficult to comprehensively analyze dynamic characteristics, including the rate, amplitude, and stability of temperature variations. Therefore, it is essential to investigate the dynamic characteristics at the diurnal scale. Across all treatments and growth stages (where the reproductive stage VT–R6 was further subdivided into VT–R3 and R3–R6 in Figure 5 to capture the canopy senescence transition), the diurnal progression of soil temperature generally exhibited a unimodal pattern, with the minimum values primarily occurring between 05:00 and 07:20, and the peak values concentrated between 14:20 and 17:00 (Figure 5). It should be noted that the precise diurnal peak and trough times were extracted directly from the raw high-frequency 20 min sensor observations prior to the hourly aggregation used for model training. Overall, the mulching treatments exerted a regulatory effect on the temperature variation phase, predominantly manifesting as a significant delay (phase shift) in the occurrence of the peak and minimum values. Regarding the peak times, the CK treatment predominantly reached its maximum between 14:20 and 16:00. In contrast, under mulched conditions, the daytime heat accumulation process was relatively gradual, leading to delayed peak occurrences. Taking the SD–VE stage as an example, compared to the CK treatment (which peaked at 15:20), the peak times for the CS, WS, and SS treatments were quantitatively delayed by 40 min (16:00), 20 min (15:40), and 100 min (17:00), respectively. As for the minimum times, although all treatments generally reached their lowest temperatures during the early morning, the mulching treatments similarly exhibited a delay effect. Specifically, during the VE–V6 stage, the minimum times for the CS and SS treatments were delayed by 40 min and 1 h, respectively, compared to the CK treatment.

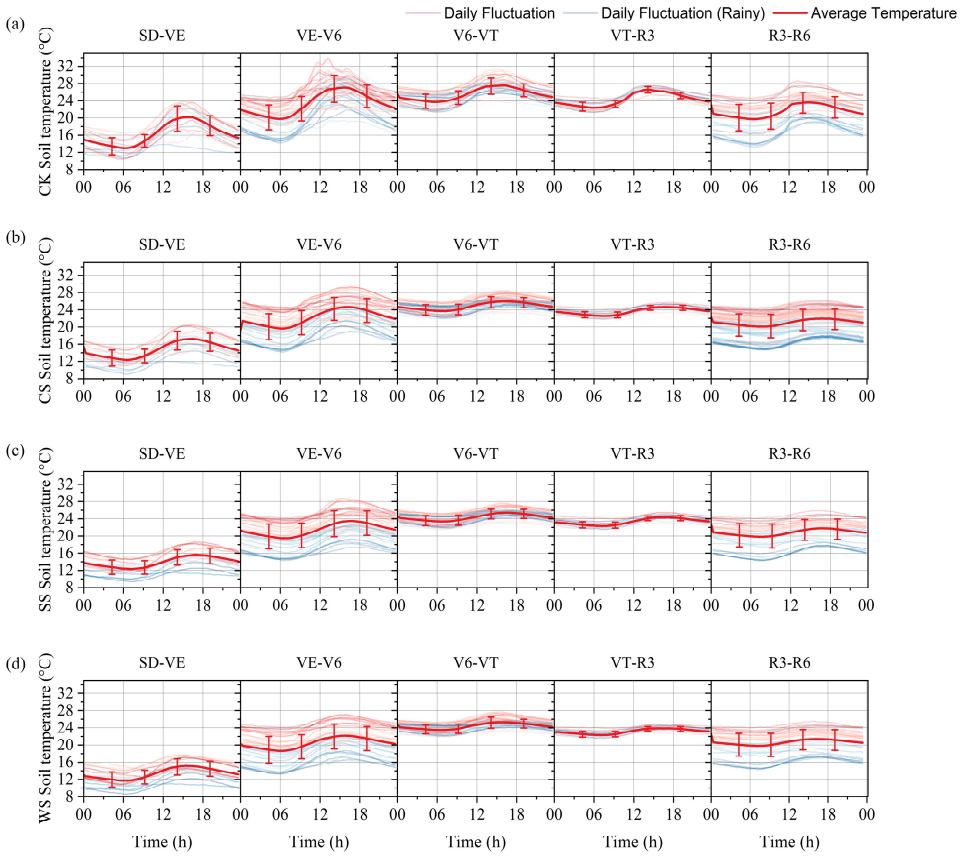


Figure 5. Diurnal dynamic characteristics of soil temperature at the 0 cm depth across different maize growth stages under various straw mulching practices: (**a**) CK, (**b**) CS, (**c**) SS, and (**d**) WS.

Regarding the diurnal amplitude (the difference between the daily maximum and minimum temperatures), the CK treatment exhibited substantial fluctuations during the early stages, recording 7.19 °C and 7.27 °C during the SD–VE and VE–V6 stages, respectively. Upon entering the V6–VT and subsequent middle and late growth stages, the amplitude decreased to 3.83–4.19 °C, indicating that the diurnal fluctuation amplitude generally converged as the growth period advanced. The mulching treatments significantly dampened the diurnal amplitude, and this dampening effect was more pronounced during the early stages. Specifically, during the SD–VE stage, the amplitudes under the CS, SS, and WS treatments were significantly reduced by approximately 32%, 54%, and 52%, respectively, compared to the CK baseline. During the VE–V6 stage, these amplitudes decreased by 25%, 45%, and 51%, respectively, relative to the CK. Throughout the middle and late stages, the mulching treatments maintained a distinct amplitude-dampening effect, with average reductions ranging from 41% to 62% compared to the CK. This demonstrates that mulching exerts a continuous buffering effect on the diurnal energy exchange in the surface soil layer, thereby resulting in flatter diurnal variation curves.

Regarding the temperature variation rate, the warming rate in this study is defined as the difference between the diurnal maximum and minimum temperatures divided by the duration of the warming process (°C·h^{-1}). The calculation results indicated that the CK treatment exhibited higher warming rates during the SD–VE and VE–V6 stages, recording 0.771 and 0.752 °C·h^{-1}, respectively. During the middle and late stages, this rate decreased to 0.348–0.483 °C·h^{-1}. The mulching treatments significantly reduced the warming rates across all stages, thereby providing a more stable thermal environment for the crop root system.

3.2. Predictive Performance Evaluation of the Hy-PINN Model

3.2.1. Correlation Between Meteorological Factors and Soil Temperature

When selecting the input variables for the model, Pearson correlation analysis (Figure 6) was employed to evaluate the degree of association between various meteorological factors and soil temperature. The soil temperature at the 0 cm depth exhibited a highly positive correlation with air temperature ($r = 0.99$), reference evapotranspiration ($r = 0.72$), and solar radiation, while showing weaker correlations with precipitation ($r = 0.29$) and relative humidity ($r = 0.15$). Although moisture factors displayed lower linear correlations, they indirectly regulate soil temperature dynamics by affecting soil thermal diffusivity from a physical mechanism perspective; therefore, they were retained in the model. Furthermore, it is particularly worth noting that although reference evapotranspiration (ET_0) is typically a comprehensively calculated value derived from basic meteorological factors—presenting a certain degree of internal multicollinearity—it serves as a high-order physical feature characterizing the potential atmospheric evaporative demand. Consequently, it more directly assists the neural network in capturing the nonlinear coupling effect of surface evaporative cooling on the thermal boundary conditions. Integrating the aforementioned statistical results and physical mechanisms, the model ultimately established a core feature set comprising seven variables: air temperature, solar radiation, precipitation, relative humidity, wind speed, reference evapotranspiration, and atmospheric pressure.

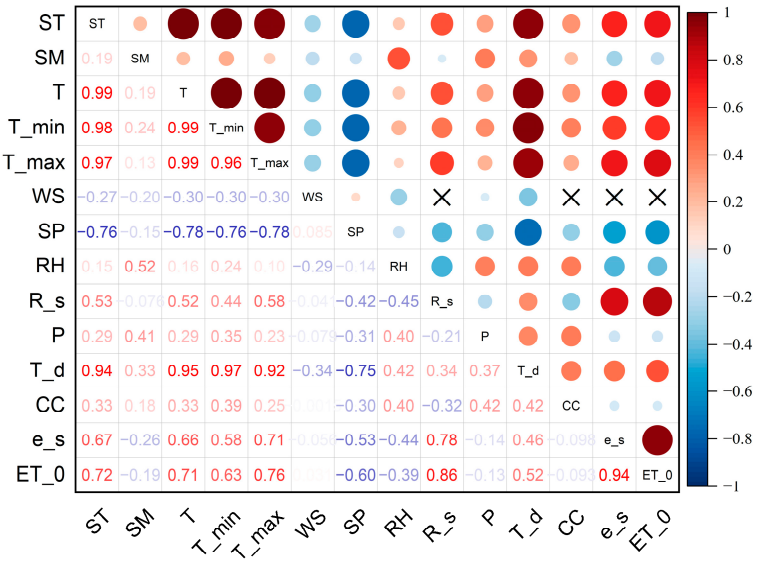


Figure 6. Pearson correlation coefficients between various meteorological factors and soil temperature at the 0 cm depth.

3.2.2. Fitting Performance of the Hy-PINN Model on the Training Set

To comprehensively evaluate the modeling capability of the Hy-PINN framework for the unsteady soil heat conduction process, a systematic analysis of the model's fitting performance at different depths was first conducted using the training dataset. Figure 7 illustrates the scatter regression results of the model at the 0 cm and 10 cm depths on the 2024 training set.

As the direct interface for soil-atmosphere energy exchange, the surface temperature is strongly driven by instantaneous variations in solar radiation and air temperature, exhibiting characteristics of high-frequency and intense fluctuations. Regression analysis revealed that on the 2024 training set, the fitting coefficients of determination (R^2) at the 0 cm depth across all treatments ranged from 0.9929 to 0.9995 (averaging 0.998), while the root mean square errors (RMSE) ranged from 0.10 to 0.39 °C (averaging 0.19 °C).

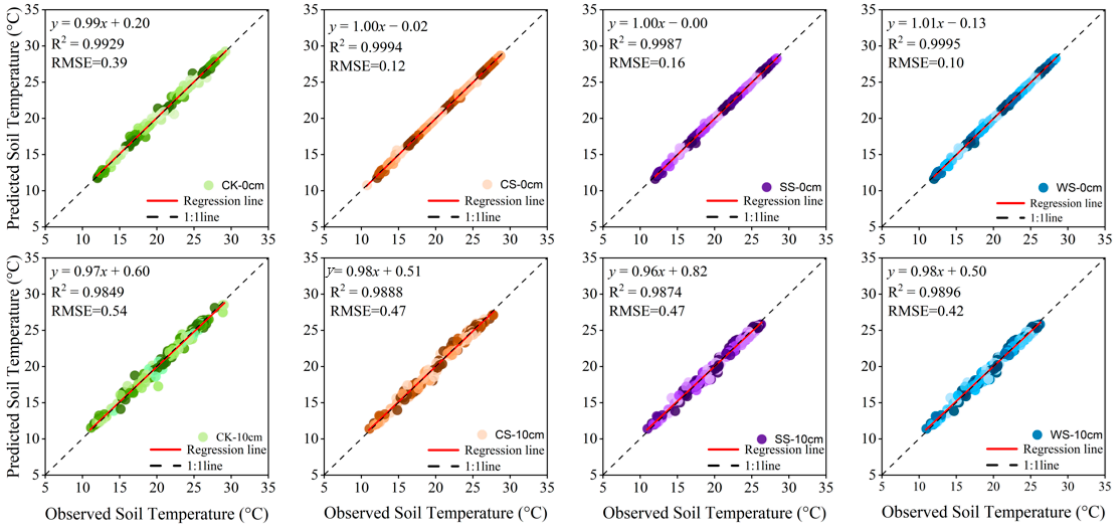


Figure 7. Scatter regression plots of the Hy-PINN model for soil temperatures at the 0 cm and 10 cm depths across the 2024 model-development dataset (N = 168 days).

Compared to the surface (0 cm), the soil temperature at the 10 cm depth exhibited distinct amplitude attenuation and phase lag characteristics in the time series. Influenced by the superimposed effects of internal soil heterogeneity, dynamic moisture fluctuations, and the downward accumulation of boundary errors during the downward heat conduction process, the fitting errors at the 10 cm depth increased relative to the surface layer. The RMSE across all treatments ranged from 0.42 to 0.54 °C (with a maximum value of 0.54 °C and an average of 0.48 °C), but the coefficient of determination (R^2) still maintained a high level, ranging from 0.9849 to 0.9896 (averaging 0.988). It is particularly worth noting that the near-perfect fitting accuracy illustrated in Figure 7 reflects the theoretical upper bound of the model's learning capacity on the training set (the 2024 data); when subsequently applied to the 2025 independent test set, the accuracy for certain treatments experienced an objective decline due to interannual climatic variability.

3.2.3. Generalization Performance of the Hy-PINN Model Under Different Mulching Conditions

Conservation tillage practices significantly alter the boundary conditions of the farmland surface energy balance by changing the physical morphology of surface mulches. To evaluate the generalization ability of the Hy-PINN framework under complex agricultural management scenarios, the predictive performance of the model was compared across four scenarios: no mulching (CK), chopped straw mulching (CS), strip tillage (SS), and whole straw mulching (WS).

As illustrated in Figures 8 and 9, the Hy-PINN framework maintained a high level of predictive performance across all four distinct surface boundaries. Influenced by the physical heterogeneity of the mulch layers, the predictive accuracy of the model at different depths exhibited gradient variations with clear physical significance.

At the 0 cm surface layer, the bare soil control (CK) exhibited the highest predictive accuracy (R^2 = 0.9532, RMSE = 0.78 °C). This is primarily because, under the no-mulching condition, the sensible heat exchange between the soil surface and the atmosphere is the most direct, enabling the Surface-DNN module to maximally capture the instantaneous driving effects of meteorological factors, such as air temperature and solar radiation, on the surface temperature. The whole straw mulching (WS) treatment ranked second (R^2 = 0.9477, RMSE = 0.89 °C); although its mulch layer was relatively thick, it formed a singular and stable physical boundary. In contrast, due to the more complex surface compositions, the predictive

accuracies for the strip tillage (SS) and chopped straw mulching (CS) treatments decreased slightly, with R^2 dropping to 0.9390 and 0.9334, respectively. Specifically, the reduction in accuracy under the SS mode can likely be attributed to the horizontal heat exchange induced by the alternating bare soil and straw strips, which intensified the nonlinear characteristics of the surface energy boundary reconstruction.

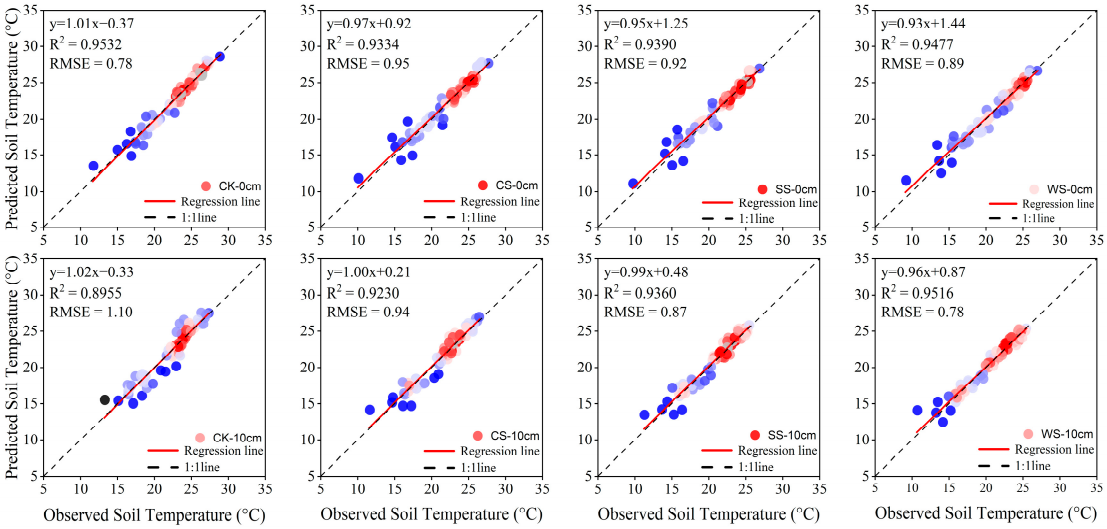


Figure 8. Comparison of the predictive accuracy of the Hy-PINN model for soil temperatures at the 0 cm and 10 cm depths under different mulching treatments (independent test set, 2025).

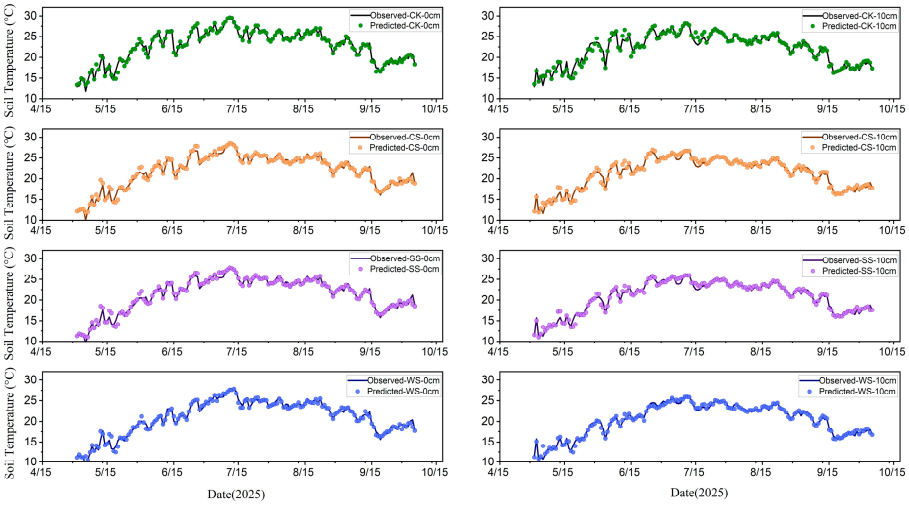


Figure 9. Validation results of the Hy-PINN model for soil temperatures at the 0 cm and 10 cm depths under different mulching treatments (independent test set, 2025).

However, at the 10 cm deep layer, the ranking of predictive accuracy exhibited a significant reversal, manifesting as the WS treatment achieving the highest accuracy (R^2 = 0.9516, RMSE = 0.78 °C), while the CK treatment recorded the lowest accuracy (R^2 = 0.8955, RMSE = 1.10 °C). This reversal elucidates the regulatory mechanism of the mulch layer on the heat diffusion process. Relying on its robust thermal insulation performance, the whole straw (WS) mulching effectively filtered out high-frequency meteorological environmental noise, rendering the temperature time-series evolution at the 10 cm depth smoother and more delayed. Such low-frequency, smooth temperature dynamics are highly compatible with the one-dimensional unsteady heat conduction equation (the physical constraint) embedded within the model, thereby yielding the optimal fitting performance. In contrast, the

CK treatment retained relatively strong high-frequency thermal fluctuations and numerous nonlinear sudden changes at the 10 cm depth, consequently increasing the difficulty for the purely physical diffusion equation to fit its dynamic trajectory.

In summary, the phenomenon of predictive accuracy reversal at the deep layer under different mulching scenarios directly demonstrates the differential impacts of the boundary conditions of each treatment on the heat conduction characteristics. Overall, the Hy-PINN framework can adaptively accommodate straw mulches of varying thicknesses and physical morphologies, thereby achieving high-precision reconstruction of the soil temperature profile under complex scenarios.

3.2.4. Comparison with the Pure Data-Driven Baseline

To rigorously demonstrate the necessity and superiority of the physics-informed constraint, a purely data-driven Deep Neural Network (DNN) baseline was evaluated. This baseline utilized the exact same network architecture and hyperparameters as the Hy-PINN, but with the heat-conduction physical loss and total variation penalty completely removed ($\lambda_{phys} = 0, \lambda_{tv} = 0$). Both models were trained exclusively on the 2024 dataset and independently tested on the unseen 2025 dataset.

As detailed in Table 2, while the standard DNN achieved acceptable accuracy at the soil surface (0 cm), its prediction error increased substantially at the 10 cm depth. For instance, the cross-year test RMSE of the DNN at 10 cm reached 1.49 °C under the SS treatment and 1.34 °C under the CK treatment. This performance degradation indicates that purely data-driven models, which rely solely on statistical correlations with meteorological inputs, struggle to accurately model downward heat propagation when applied to unseen weather patterns. In contrast, by explicitly embedding the thermal relaxation governing equation, the proposed Hy-PINN enforces strict thermodynamic consistency across soil layers. Consequently, the Hy-PINN consistently outperformed the baseline DNN across all treatments, effectively reducing the 10 cm test RMSE and maintaining it below 1.10 °C (with MAE similarly reduced). This direct comparison confirms that the data-physics dual-driven mechanism fundamentally enhances the structural robustness and cross-year generalization capability of the model, robustly proving the dual-mechanism advantage. Crucially, the performance gain of Hy-PINN over the baseline DNN is not merely an artifact of generic numerical smoothing. Generic temporal smoothing (such as L_2 or total-variation filtering on temperature outputs) acts as a low-pass filter that indiscriminately attenuates peak amplitudes without correcting phase timing. In contrast, the embedded heat-transfer relaxation constraint explicitly couples the temporal derivative $\frac{dT_{10}}{dt}$ to the vertical thermal gradient $[T_0(t) - T_{10}(t)]$. Physically, this dictates that the 10 cm temperature can only rise when $T_0 > T_{10}$ and must peak precisely when the downward heat flux reverses ($T_0 = T_{10}$). Consequently, while the baseline DNN exhibits synchronous, unphysical temperature jumps at 10 cm during abrupt weather shifts, the Hy-PINN accurately reproduces both the asymmetric diurnal phase lag (2–3 h) and the amplitude attenuation ratio between 0 cm and 10 cm. Furthermore, to visually expose model behaviors regarding synoptic weather-event responses as well as diurnal amplitude and phase timing, multi-scale validation windows from the unseen 2025 test set (including multiple rainfall-induced cooling events at both daily and hourly resolutions) are presented in Figure 10, alongside an ablation variant with generic temporal smoothing. The "DNN + Smoothing" baseline was constructed by entirely removing the heat-conduction physical loss and the total variation penalty ($\lambda_{phys} = 0, \lambda_{tv} = 0$). Instead, to simulate a generic mathematical smoothing effect without physical coupling, a first-order temporal difference penalty was introduced into the loss function: $\mathcal{L}_{smooth} = \frac{1}{N-1}\sum_{t=1}^{N-1}\left[\left(\hat{T}_0(t+1) - \hat{T}_0(t)\right)^2 + \left(\hat{T}_{10}(t+1) - \hat{T}_{10}(t)\right)^2\right]$. To ensure a fair comparison regarding gradient magnitudes, the weighting coefficient for this generic

smoothing term was set to $\lambda_{smooth} = 1.0$ (identical to the physical weight λ_{phys}). As shown in Figure 10 and Table 2, generic smoothing indiscriminately flattens diurnal peak amplitudes and induces severe phase trailing that degrades 10 cm accuracy (e.g., increasing 10 cm RMSE from 1.34 °C to 1.38 °C under CK and from 1.49 °C to 1.52 °C under SS), whereas the Hy-PINN accurately captures both the conductive damping during rainfall events (Figure 10a,b) and the 2–3 h asymmetric diurnal phase lag across soil layers (Figure 10c,d).

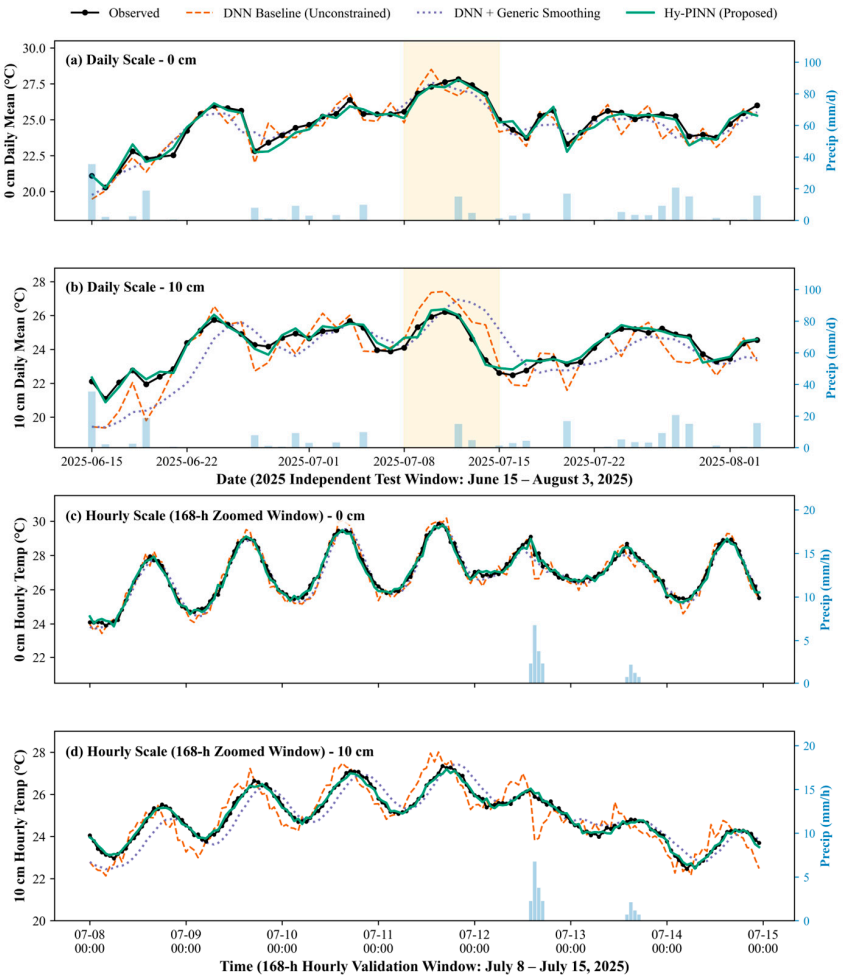


Figure 10. Multi-scale validation windows on the unseen 2025 independent test set (under the SS treatment) comparing Observed, unconstrained DNN Baseline, DNN + Generic Smoothing, and the proposed Hy-PINN model: (**a**,**b**) multi-week daily trajectory from 15 June to 3 August 2025 at 0 cm and 10 cm depths with daily precipitation; (**c**,**d**) zoomed-in 168 h hourly validation window (8 July to 15 July 2025) exposing diurnal amplitude attenuation, the 2–3 h phase lag, and hourly responses to a rainfall cooling event.

Table 2. Cross-year performance comparison between the pure DNN baseline and the proposed Hy-PINN model on the 2025 independent test set.

Treatment	Depth	Model	RMSE (°C)	R^2	MAE (°C)
CK	0 cm	DNN Baseline	1.07	0.9119	0.82
		DNN + Smoothing	1.04	0.9168	0.81
		Hy-PINN	0.78	0.9532	0.61
	10 cm	DNN Baseline	1.34	0.8449	1.02
		DNN + Smoothing	1.38	0.8355	1.12
		Hy-PINN	1.10	0.8955	0.86

Table 2. *Cont.*

Treatment	Depth	Model	RMSE (°C)	R^2	MAE (°C)
CS	0 cm	DNN Baseline	1.09	0.9123	0.84
		DNN + Smoothing	1.08	0.9139	0.83
		Hy-PINN	0.95	0.9334	0.75
	10 cm	DNN Baseline	1.12	0.8907	0.87
		DNN + Smoothing	1.15	0.8848	0.93
		Hy-PINN	0.94	0.9230	0.76
SS	0 cm	DNN Baseline	1.39	0.8608	1.05
		DNN + Smoothing	1.34	0.8706	1.03
		Hy-PINN	0.92	0.9390	0.73
	10 cm	DNN Baseline	1.49	0.8122	1.13
		DNN + Smoothing	1.52	0.8045	1.24
		Hy-PINN	0.87	0.9360	0.69
WS	0 cm	DNN Baseline	1.19	0.9065	0.91
		DNN + Smoothing	1.16	0.9112	0.90
		Hy-PINN	0.89	0.9477	0.72
	10 cm	DNN Baseline	1.30	0.8654	1.01
		DNN + Smoothing	1.35	0.8549	1.11
		Hy-PINN	0.78	0.9516	0.64

4. Discussion

4.1. Regulatory Mechanisms of Different Mulching Treatments on Soil Temperature

Field observations and model simulations in this study consistently demonstrated that the regulation of soil temperature by straw mulching exerts significant dual effects of cooling and heat preservation, which are jointly influenced by the physical morphology of the mulch and the crop growth stage. By forming a continuous thermal insulation layer, the whole straw mulching (WS) treatment exhibited the strongest cooling effect. Conversely, the chopped straw mulching (CS) treatment displayed the weakest cooling effect owing to its loose structure, which allows for partial energy penetration. Meanwhile, the cooling effect of the strip tillage (SS) treatment was intermediate between the two.

Notably, the cooling effect of the mulching treatments was primarily concentrated during the seedling stages (the SD–VE and VE–V6 stages), a period when the crop is most sensitive to temperature. For instance, the average soil temperature during the emergence stage (SD–VE) under the WS treatment in 2025 was only 13.52 °C, which closely approached the minimum critical temperature for maize emergence (12 °C). This indicates that in the cold regions of Northeast China, straw mulching acts as a double-edged sword: if the whole straw mulching (WS) applied in spring is excessively thick, it is highly susceptible to inducing cold stress, thereby increasing the risk of delayed emergence and poor seedling vigor. Conversely, upon entering the high-temperature summer period (the V6–VT stage), the continuous cooling and buffering effect (approximately 1–2 °C) exerted by the mulching treatments can effectively mitigate the heat stress beneath the canopy and reduce excessive soil moisture evaporation.

In this context, strip tillage (SS) exhibited a high degree of agronomic suitability. Its magnitude of temperature reduction during the seedling stage was significantly smaller than that of the WS treatment, whereas its cooling and buffering effect during the summer was comparable to that of the WS treatment. The underlying physical mechanism can be attributed to its unique structural characteristics: during the spring seedling stage, the bare soil strips under the SS mode directly receive solar radiation, forming localized

warming channels and facilitating the rapid recovery of deep soil temperatures. In summer, coupled with maize canopy closure and the physical shading provided by the straw strips, it offers excellent thermal buffering for the root zone. From an agronomic perspective, these spatial complementary traits suggest potential agronomic benefits for expanding the safe sowing window and supporting late-maturing cultivars in the high-latitude cold regions of Northeast China, though direct crop responses warrant further physiological validation.

4.2. Dual-Driven Advantages of the Hy-PINN Model and Comparison with Traditional Models

The results of this study revealed that the predictive accuracy of the model at the surface layer (0 cm) followed the sequence of CK > WS > SS > CS, whereas at the deep layer (10 cm), it significantly reversed to WS > SS > CS > CK. This accuracy reversal phenomenon should not be merely regarded as error fluctuation; rather, it profoundly corroborates the dual-mechanism advantage of the Hy-PINN model: shallow-layer data-driven learning and deep-layer physical optimization. At the bare soil (CK) surface layer, the sensible heat exchange is intense, allowing the Surface-DNN module to sensitively capture the instantaneous nonlinear driving effects of meteorological factors. Conversely, at the deep layer under the WS treatment, the robust thermal insulation layer substantially filtered out high-frequency thermal noise. Such a low-frequency and smooth heat diffusion process is highly compatible with the one-dimensional unsteady heat conduction equation (PDE) embedded within the model, thereby enabling the physical constraints to effectively guide the predictive trajectory.

Compared to traditional mechanistic models and purely data-driven models, the Hy-PINN framework exhibits distinct advantages in complex unsteady agricultural scenarios. First, traditional physical models (e.g., HYDRUS-1D and SHAW) are highly dependent on physical parameters that are exceedingly difficult to acquire in real time, such as the porosity and thermal conductivity of the mulch layer. In complex straw mulching scenarios lacking precise parameter calibration, traditional mechanistic models often suffer from significant error accumulation in predicting deep soil temperatures due to the strong spatiotemporal variability of mulch thermal properties. In contrast, the Hy-PINN framework adaptively inverts the thermal diffusivity through a dedicated parameter projection branch, thereby eliminating the reliance on measured soil-water parameters and robustly controlling the RMSE of deep-layer predictions to within 1.10 °C.

Second, as demonstrated by the baseline evaluation in Section 3.2.4, purely data-driven models lack physical regularization. Under extreme weather conditions characterized by high-frequency meteorological noise or dry-wet cycles, standard deep learning models are highly susceptible to generating abrupt temperature predictions that violate thermodynamic laws [18]. In contrast, the PDE embedded within the Hy-PINN framework serves as a physical constraint, guiding the predictive trajectory toward the feasible domain of energy conservation. Even during periods of drastic fluctuations induced by heavy rainfall, the Hy-PINN framework maintains robust phase synchronization and effectively mitigates non-physical oscillations. While existing models have achieved high predictive accuracy under idealized boundary conditions [30], this study further demonstrates that PINNs possess remarkable generalization capabilities even under the highly heterogeneous boundaries of straw mulching.

To further elucidate the physical mechanism learned by the Hy-PINN, the temporal dynamics of the inferred apparent thermal diffusivity (κ) during the 2024 growing season were visualized (Figure 11). Rescaled to standard physical units, κ varied smoothly between 1.13×10^{-6} and 1.40×10^{-6} $m^2 \cdot s^{-1}$, corresponding to a realistic conductive relaxation time ($\tau = \Delta z^2/\kappa$) of 1.98–2.46 h across the 0–10 cm topsoil layer. The extracted curves exhibited smooth, continuous intra-seasonal variations rather than erratic non-physical

fluctuations, proving the efficacy of the model's design. Notably, the whole straw mulching (WS) treatment consistently maintained the highest apparent thermal diffusivity. This physically aligns with the field reality that full-scale mulching optimally preserves soil moisture, and higher water content fundamentally enhances soil thermal conduction capabilities. Conversely, the CK, CS, and SS treatments exhibited lower values due to intensified surface evaporation. This demonstrates that the Hy-PINN successfully captured the distinct thermodynamic boundary behaviors of different mulching morphologies purely from data-physics dual-driven learning.

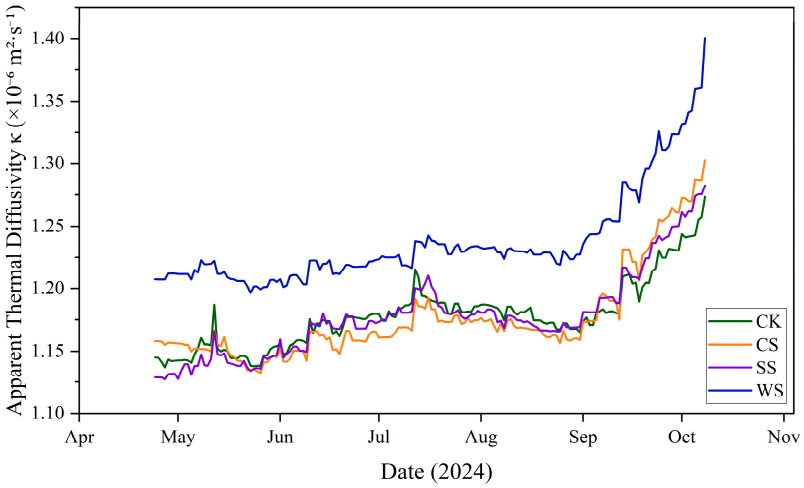


Figure 11. Temporal dynamics of the apparent thermal diffusivity (κ, $\times 10^{-6}$ $m^2 \cdot s^{-1}$) inverted by the Hy-PINN model under different straw mulching treatments (CK, CS, SS, and WS) during the 2024 growing season.

4.3. Limitations and Future Prospects

Although the Hy-PINN model developed in this study exhibited high predictive accuracy when handling different straw mulching scenarios, several limitations still exist regarding the simplification of physical assumptions and the treatment of boundary conditions. First, the physical constraints in this study were constructed based on the one-dimensional vertical heat conduction equation, which fails to capture the lateral heat flux between the bare soil strips and the mulched strips under the strip tillage (SS) mode. This is likely one of the primary reasons for the slightly higher predictive errors at the deep layer under this treatment. Second, the soil during the spring sowing period in Northeast China is often subjected to alternating freeze–thaw cycles. Currently, the model has not explicitly embedded the latent heat exchange induced by the phase change process. Although the data-driven component may have implicitly learned these features to some extent, the lack of an explicit physical description restricts the physical interpretability of the model under extremely low-temperature conditions. Furthermore, because the inversion of the thermal diffusivity (κ) heavily relies on the attenuation characteristics of temperature waves, the time-series estimation of κ may experience transient numerical oscillations when soil moisture undergoes severe variations (such as heavy rainfall infiltration).

To address the aforementioned limitations, future research could be advanced and refined across the following dimensions. Regarding mechanistic enhancements, future models should incorporate a two-dimensional partial differential equation for heat conduction (2D-PDE) to explicitly simulate the lateral heat flux under complex spatial structures such as strip tillage (SS). Additionally, embedding a freeze–thaw phase change module would comprehensively improve the model's applicability in cold-region agriculture. Regarding algorithmic optimization, exploring more efficient forms of physical constraints (e.g.,

Neural Ordinary Differential Equations, Neural ODEs) is recommended to further reduce the computational cost of the model under complex unsteady boundaries. Furthermore, future studies could couple the high-precision soil temperature time-series data generated by the Hy-PINN framework as driving parameters into crop growth models, such as DSSAT or AquaCrop, thereby directly quantifying the impacts of different mulching treatments on crop biomass and final yield. Regarding the specific technical route for this coupling, the primary challenges in this direction lie in resolving the temporal upscaling conversion between the high-frequency (hourly) micrometeorological outputs of the Hy-PINN model and the macroscopic (daily) time steps of traditional crop models, as well as overcoming the barriers between physics-informed neural networks and traditional mechanistic models concerning parameter interfaces and data assimilation.

5. Conclusions

This study quantified the thermal effects of straw mulching practices and proposed a hybrid physics-informed neural network (Hy-PINN). Mulching exhibited a significant phase-dependent cooling effect, primarily during the spring seedling stage. Strip tillage (SS) provided a balanced thermal environment, mitigating the early-spring cold stress risk of whole straw mulching. The Hy-PINN effectively overcame traditional physical models' reliance on parameterized soil boundaries by dynamically reconstructing surface boundary temperatures and inverting apparent thermal diffusivity from routine meteorological inputs. Independent cross-year testing confirmed its robust generalization capability across heterogeneous mulching scenarios. While relying on a simplified thermal relaxation assumption, the Hy-PINN serves as an accurate and cost-effective virtual sensing tool to complement field monitoring, offering valuable insights for regional conservation tillage optimization.

Author Contributions: F.Z. and D.X. developed the software and wrote the original draft. F.Z. also contributed to reviewing and editing the manuscript. B.C. and J.X. performed the validation. R.Z. was responsible for supervision, project administration, and funding acquisition. All authors have read and agreed to the published version of the manuscript.

Funding: This work was supported by the National Natural Science Foundation of China (Grant No. 32301689).

Institutional Review Board Statement: Not applicable. This study does not involve human participants, animals, or endangered plant species.

Informed Consent Statement: Not applicable.

Data Availability Statement: The data presented in this study are available on request from the corresponding author. The data are not publicly available due to ongoing research.

Acknowledgments: The authors would like to thank our lab colleagues for their assistance in field data collection and equipment maintenance.

Conflicts of Interest: The authors declare no conflicts of interest.

References

1. Licht, M.A.; Al-Kaisi, M. Strip-Tillage Effect on Seedbed Soil Temperature and Other Soil Physical Properties. *Soil Tillage Res.* **2005**, *80*, 233–249. [CrossRef]
2. Stone, P.J.; Sorensen, I.B.; Jamieson, P.D. Effect of Soil Temperature on Phenology, Canopy Development, Biomass and Yield of Maize in a Cool-Temperate Climate. *Field Crops Res.* **1999**, *63*, 169–178. [CrossRef]
3. Chen, S.Y.; Zhang, X.Y.; Pei, D.; Sun, H.Y.; Chen, S.L. Effects of Straw Mulching on Soil Temperature, Evaporation and Yield of Winter Wheat: Field Experiments on the North China Plain. *Ann. Appl. Biol.* **2007**, *150*, 261–268. [CrossRef]
4. Sarkar, S.; Singh, S. Interactive Effect of Tillage Depth and Mulch on Soil Temperature, Productivity and Water Use Pattern of Rainfed Barley (*Hordium vulgare* L.). *Soil Tillage Res.* **2007**, *92*, 79–86. [CrossRef]

5. Zhao, J.; Lu, Y.; Tian, H.; Jia, H.; Guo, M. Effects of Straw Returning and Residue Cleaner on the Soil Moisture Content, Soil Temperature, and Maize Emergence Rate in China's Three Major Maize Producing Areas. *Sustainability* **2019**, *11*, 5796. [CrossRef]
6. Wang, C.; Ai, S.; Chen, Q.; Li, J.; Ding, J.; Yang, F. Effect of Strip Tillage Widths on Soil Moisture, Soil Temperature and Soil Structure in Northeast China. *Front. Environ. Sci.* **2024**, *12*, 1404971. [CrossRef]
7. Bollero, G.A.; Bullock, D.G.; Hollinger, S.E. Soil Temperature and Planting Date Effects on Corn Yield, Leaf Area, and Plant Development. *Agron. J.* **1996**, *88*, 385–390. [CrossRef]
8. Onwuka, B. Effects of Soil Temperature on Some Soil Properties and Plant Growth. *Adv. Plants Agric. Res.* **2018**, *8*, 34–37. [CrossRef]
9. Šimůnek, J.; Van Genuchten, M.T.; Šejna, M. Recent Developments and Applications of the HYDRUS Computer Software Packages. *Vadose Zone J.* **2016**, *15*, 1–25. [CrossRef]
10. Flerchinger, G.N.; Saxton, K.E. Simultaneous Heat and Water Model of a Freezing Snow-Residue-Soil System I. Theory and Development. *Trans. ASAE* **1989**, *32*, 0565–0571. [CrossRef]
11. Deardorff, J.W. Efficient Prediction of Ground Surface Temperature and Moisture, with Inclusion of a Layer of Vegetation. *J. Geophys. Res.* **1978**, *83*, 1889–1903. [CrossRef]
12. Mady, A.Y.; Shein, E. Estimating Soil Thermal Diffusivity Using Pedotransfer Functions with Nonlinear Regression. *Open Agric. J.* **2018**, *12*, 164–173. [CrossRef]
13. Peng, P.; Liu, L.; Arkhangelskaya, T.A.; Mady, A.Y.; Dyck, M.; Zvomuya, F.; He, H. Random Forest Approach to Estimate Soil Thermal Diffusivity: Evaluation and Comparison with Traditional Pedotransfer Functions. *Soil Tillage Res.* **2024**, *244*, 106233. [CrossRef]
14. Feng, Y.; Cui, N.; Hao, W.; Gao, L.; Gong, D. Estimation of Soil Temperature from Meteorological Data Using Different Machine Learning Models. *Geoderma* **2019**, *338*, 67–77. [CrossRef]
15. Sit, M.; Demiray, B.Z.; Xiang, Z.; Ewing, G.J.; Sermet, Y.; Demir, I. A Comprehensive Review of Deep Learning Applications in Hydrology and Water Resources. *Water Sci. Technol.* **2020**, *82*, 2635–2670. [CrossRef] [PubMed]
16. Kashinath, K.; Mustafa, M.; Albert, A.; Wu, J.-L.; Jiang, C.; Esmaeilzadeh, S.; Azizzadenesheli, K.; Wang, R.; Chattopadhyay, A.; Singh, A.; et al. Physics-Informed Machine Learning: Case Studies for Weather and Climate Modelling. *Phil. Trans. R. Soc. A* **2021**, *379*, 20200093. [CrossRef] [PubMed]
17. Reichstein, M.; Camps-Valls, G.; Stevens, B.; Jung, M.; Denzler, J.; Carvalhais, N. Prabhat Deep Learning and Process Understanding for Data-Driven Earth System Science. *Nature* **2019**, *566*, 195–204. [CrossRef] [PubMed]
18. Willard, J.; Jia, X.; Xu, S.; Steinbach, M.; Kumar, V. Integrating Scientific Knowledge with Machine Learning for Engineering and Environmental Systems. *ACM Comput. Surv.* **2023**, *55*, 1–37. [CrossRef]
19. Cai, S.; Wang, Z.; Wang, S.; Perdikaris, P.; Karniadakis, G.E. Physics-Informed Neural Networks for Heat Transfer Problems. *J. Heat Transf.* **2021**, *143*, 060801. [CrossRef]
20. Karniadakis, G.E.; Kevrekidis, I.G.; Lu, L.; Perdikaris, P.; Wang, S.; Yang, L. Physics-Informed Machine Learning. *Nat. Rev. Phys.* **2021**, *3*, 422–440. [CrossRef]
21. Tartakovsky, A.M.; Marrero, C.O.; Perdikaris, P.; Tartakovsky, G.D.; Barajas-Solano, D. Physics-Informed Deep Neural Networks for Learning Parameters and Constitutive Relationships in Subsurface Flow Problems. *Water Resour. Res.* **2020**, *56*, e2019WR026731. [CrossRef]
22. Xie, X.; Yan, H.; Lu, Y.; Zeng, L. Simulating Field Soil Temperature Variations with Physics-Informed Neural Networks. *Soil Tillage Res.* **2024**, *244*, 106236. [CrossRef]
23. Ran, C.; Gao, D.; Bai, T.; Geng, Y.; Shao, X.; Guo, L. Straw Return Alleviates the Negative Effects of Saline Sodic Stress on Rice by Improving Soil Chemistry and Reducing the Accumulation of Sodium Ions in Rice Leaves. *Agric. Ecosyst. Environ.* **2023**, *342*, 108253. [CrossRef]
24. Song, F.; Liu, M.; Zhang, Z.; Qi, Z.; Li, T.; Du, S.; Li, A.; Liu, J. No-Tillage with Straw Mulching Increased Maize Yield and Nitrogen Fertilizer Recovery Rate in Northeast China. *Agric. Water Manag.* **2024**, *292*, 108687. [CrossRef]
25. Carslaw, H.S.; Jaeger, J.C. *Conduction of Heat in Solids*, 2nd ed.; Clarendon Press: Oxford, UK; Oxford University Press: Oxford, UK; Oxfordshire, UK; New York, NY, USA, 1986; ISBN 978-0-19-853368-9.
26. Wu, Z.; Zhu, Y.; Cui, Y.; Li, Q.; Cheng, Y.; Li, R.; Willcock, S.; Storkey, J.; Vona, V.; Vér, A.; et al. Long-Term Straw Mulching Enhanced Topsoil Fertility and Improved Yield Stability and Sustainability in Soybean Production. *J. Integr. Agric.* **2026**, S209531192600153X. [CrossRef]
27. Zizinga, A.; Chemura, A.; Ruane, A.C.; Tietjen, B. Straw Mulching Enhances Rainfed Maize Yield under Climate Change Scenarios. *Eur. J. Agron.* **2026**, *172*, 127827. [CrossRef]
28. Lu, Y.; Huo, H.; Deng, F.; Yang, Y.; He, H.; Xie, H.; Zhang, X.; Bao, X. Trade-Offs between Maize Yield and Soil Fertility under Different Straw Mulching Amounts in No-Tillage Systems: Evidence from a 15-Year Experiment in Northeast China. *Field Crops Res.* **2026**, *342*, 110479. [CrossRef]

29. Wang, Y.; Ji, Y.; Ma, J.; Elena, M.; Assiya, A.; Ding, R.; Jia, Z.; Siddique, K.H.M.; Liu, E.; He, J.; et al. Evaluate the Impacts of Different Straw Returning Rates on Soil Quality and Field Environmental Sustainability of Film Mulching or Non-Mulching Farmland in Semiarid Region. *Environ. Res.* **2025**, *285*, 122483. [CrossRef] [PubMed]
30. Raissi, M.; Perdikaris, P.; Karniadakis, G.E. Physics-Informed Neural Networks: A Deep Learning Framework for Solving Forward and Inverse Problems Involving Nonlinear Partial Differential Equations. *J. Comput. Phys.* **2019**, *378*, 686–707. [CrossRef]

Disclaimer/Publisher's Note: The statements, opinions and data contained in all publications are solely those of the individual author(s) and contributor(s) and not of MDPI and/or the editor(s). MDPI and/or the editor(s) disclaim responsibility for any injury to people or property resulting from any ideas, methods, instructions or products referred to in the content.